Chemical Engineering Journal 490 (2024) 151405

Contents lists available at ScienceDirect

Chemical Engineering Journal

journal homepage: www.elsevier.com/locate/cej

Enhancing thermoelectric performance of solution-processed polycrystalline SnSe with PbSe nanocrystals

Yu Liu [a,b,1], Seungho Lee [b,1], Christine Fiedler [b], Maria Chiara Spadaro [c], Cheng Chang [b,d], Mingquan Li [a], Min Hong [e], Jordi Arbiol [c,f], Maria Ibáñez [b,*]

[a] Anhui Province Engineering Research Center of Flexible and Intelligent Materials, School of Chemistry and Chemical Engineering, Hefei University of Technology, 230009 Hefei, China
[b] Institute of Science and Technology Austria (ISTA), Am Campus 1, 3400 Klosterneuburg, Austria
[c] Catalan Institute of Nanoscience and Nanotechnology (ICN2), CSIC and BIST, Campus UAB, Bellaterra, 08193 Barcelona, Catalonia, Spain
[d] School of Materials Science and Engineering, Beihang University, Beijing 100191, China
[e] Centre for Future Materials and School of Engineering, University of Southern Queensland, Springfield Central, Queensland 4300, Australia
[f] ICREA, Pg. Lluís Companys 23, Barcelona, Catalonia, 08010, Spain

ARTICLE INFO

Keywords:
Tin selenide
Nanocomposites
Solution processing
Thermoelectricity
Thermal conductivity

ABSTRACT

There is a growing interest in cost-effective polycrystalline SnSe-based thermoelectric (TE) materials, which are able to replace the high performance but mechanically fragile and costly single-crystalline SnSe. In this study, we present a low-temperature solution-based approach to produce SnSe-PbSe nanocomposites with outstanding TE performance. Our method involves combining surfactant-free SnSe particles with oleate-capped PbSe nanocrystals in specific ratios, followed by thermal annealing and consolidation using spark plasma sintering. These nanocomposites are characterized by distinct compositional and structural properties that significantly impact their transport properties. In particular, the addition of oleate-capped PbSe nanocrystals results in: i) a reduction in the electrostatically adsorbed Na at the surface of the SnSe particles; ii) a reduction of Sn vacancies due to alloying with Pb; iii) an increase in grain boundary density; and iv) the formation of PbSnSe secondary phases. Notably, the SnSe-2.5 %PbSe nanocomposites demonstrate a 30 % decrease in thermal conductivity compared to that of the SnSe matrix. This reduction contributes to a maximum figure of merit (zT) of 1.75 at 788 K with a high average zT value of *ca.* 1.2 in the medium temperature range of 573–773 K. These values represent one of the highest reported in polycrystalline SnSe materials, showcasing the potential of our fabricated SnSe-PbSe nanocomposites for cost-effective TE applications.

1. Introduction

Thermoelectric (TE) devices enable direct and reversible conversion between thermal and electrical energy. Their energy conversion efficiency depends on a material's dimensionless parameter known as the TE figure of merit, $zT = \sigma S^2 T / \kappa$, where S is the Seebeck coefficient, σ denotes electrical conductivity, κ represents thermal conductivity, and T is the absolute temperature [1–4]. To produce high performance devices, the TE material must have high σ, large S, and low κ. However, the interdependence among these parameters makes it challenging to optimize them to yield a high zT [1,3].

Medium-temperature TE devices, which are proposed for recovering heat from a variety of sources such as combustion engine exhausts [5], high-temperature catalytic crackers [6], and furnaces [7], to cite just a few, highlight the potential of these technologies in efficiently utilizing waste heat. Over the last decade, SnX-based (X = S, Se, Te) binary chalcogenides have garnered significant interest for medium-temperature TE applications [8], specially SnSe [9,10]. Ultra-high zT values for both *p*- [11] and *n*-type [12] single-crystals have been reported along a particular crystallographic direction. Proof-of-concept devices based on these materials have since been fabricated, hinting at their viable real-world applications [13,14]. However, the challenges associated with the processing and mechanical stability of single-crystal SnSe, impede their use for large-scale practical applications [15,16].

* Corresponding author.
E-mail address: mibanez@ist.ac.at (M. Ibáñez).
[1] These authors contributed equally to this work.

https://doi.org/10.1016/j.cej.2024.151405
Received 30 January 2024; Received in revised form 18 March 2024; Accepted 16 April 2024
Available online 17 April 2024

Hence, producing polycrystalline SnSe with similar performance is imperative.

To date, polycrystalline SnSe has shown moderate TE performance, primarily due to two reasons: 1) its carrier mobility (μ) is substantially lower, resulting in a significantly reduced average zT (zT_{avg}) values in the low-to-mid temperature range [16]; and 2) the formation of an oxidized SnO_x layer at the surfaces resulting in high κ [9,17–19]. Thus, despite the advantage of phonon scattering as a result of the high grain boundary density in polycrystalline SnSe, these materials tend to show larger thermal conductivities than the single crystal counterpart.

To address the above challenges and promote the TE performance of polycrystalline SnSe, novel strategies have been developed, including stoichiometry control [20–22], doping [23–36], alloying [37–39], removing surface oxides [17,18], and tuning nanostructuration [40–44]. These methods have facilitated significant improvements in the zT values of polycrystalline SnSe synthesized by both solid-state and solution-processing techniques. In comparison with the solid-phase approach, solution-processing methods have been successfully applied in numerous systems, yielding superior zT values [20–23,27,28,30,31,39,42,44,45]. The excellent performance obtained using facile, scalable, potentially low-cost, high-yield, and versatile nanoparticle-based bottom-up processing approaches is attributed to the nanometer scale control over crystallite size, facets, orientation, and phase distribution, improving the carrier scattering mechanism at the grain boundaries and optimizing the electrical transport while maintaining low κ [46,47].

In this study, we present a simple and versatile method to fabricate SnSe nanocomposites (NCPs) with tailored compositions and enhanced TE performance. Specifically, we combine oleate-capped PbSe nanocrystals (NCs) with SnSe powders synthesized through an aqueous method, resulting in SnSe-PbSe NCPs. The integration of PbSe NCs into the SnSe powder allows for composition and microstructure control during the consolidation process, resulting in nanocomposites with significantly reduced κ compared to the pristine SnSe matrix across the entire temperature range. This approach yields highly stable polycrystalline SnSe materials with consistently high zT_{avg} values in the mid-temperature range. This study underscores the efficacy of producing nanocomposites for efficient utilization in TE applications through cost-effective and versatile methods.

2. Results and discussion

Surfactant-free SnSe particles are synthesized by a cost-effective and simple method at ambient pressure, using deionized water as solvent, and inexpensive $SnCl_2{\cdot}H_2O$ and Se powder as precursors [48]. The as-synthetized SnSe particles are washed through several leaching cycles with deionized water and ethanol by precipitation/redispersion, followed by vacuum drying overnight at room temperature [49]. Afterwards, the dried SnSe powder is annealed in forming gas (95 % N_2 + 5 % H_2) to remove oxide species on the particle surface [17,19]. For the evaluation of TE properties, the annealed powders are consolidated into cylindrical pellets with a diameter of Ø = 9 mm and a thickness of h = 12 mm under vacuum, using spark plasma sintering (SPS). Additional details of the entire process can be found in the supporting information (SI).

Morphological analysis of the SnSe particles is performed using scanning electron microscopy (SEM) and transmission electron microscopy (TEM), which show rectangular particles with an average size of 150 ± 50 nm (Fig. S1), consistent with the previous report [49]. To produce SnSe-x%PbSe (x mol%, x = 0, 1.5, 2.0, 2.5) NCPs, 4.0 g of SnSe particles are mixed with different amounts of PbSe NCs in anhydrous hexane. Oleate-capped PbSe NCs are prepared following a previously reported procedure [50], which yield uniform quasi-spherical particles with a narrow size distribution centered at 5.5 nm (Fig. S2). The mixtures are vigorously stirred at room temperature in an N_2-filled vial for *ca.* 2 h. After 2 h under magnetic stirring, the colloidal stability of the PbSe dispersion is wrecked, resulting in the formation of SnSe-PbSe precipitates (Fig. S3). The SnSe-x%PbSe particle blend is removed from the solution by discarding the supernatant. The remaining powder is then washed with fresh ethanol, and dried under vacuum, to yield fine powders with a homogeneous distribution of PbSe NCs in between the SnSe particles (Fig. S4). The complete process used to produce the NCPs is schematically shown in Fig. 1.

Previously, we demonstrated that particles produced in polar solvents have electrostatically charged Na ions adsorbed on the surface to achieve charge neutrality [49]. We also demonstrated that if Na was present as a surface adsorbate it would end up within the crystal lattice as a dopant. Since its concentration surpasses the solubility limit in the final bulk SnSe, Na segregates in dislocations, precipitates, and the formation of grain boundary complexions [49]. Herein, we show that mixing SnSe powders with oleate-capped PbSe NCs reduces the total amount of Na in the final material. This reduction occurs through the formation of Na oleate, which is then leached out during the ethanol washing steps (Fig. 2a–b) [51], influencing the transport properties in SnSe-PbSe NCPs, as discussed below. The removal of Na is evidenced by ^{1}H NMR analysis of the two supernatants collected after washing the SnSe-PbSe particles, which indicates the presence of oleate in both washes (Fig. 2c). Moreover, Na is detected in the supernatant through energy dispersive X-ray spectroscopy (EDX) as show in Fig. S5.

Following the same steps as for the SnSe pellet, the SnSe-x%PbSe powders are first annealed in a reducing atmosphere and then consolidated into SnSe-PbSe cylindrical pellets. The overall composition of the consolidated SnSe-x%PbSe (x mol%, x = 0, 1.5, 2.0, 2.5) pellets matches the nominal SnSe-x%PbSe particle mixtures used as indicated by EDX data (Fig. S6). Independent of the initial presence of PbSe, all pellets have similar relative densities, *ca.* 93–95 % of their theoretical value (Table S1).

All X-ray diffraction (XRD) patterns of SnSe-x%PbSe (x = 0, 1.5, 2.0 and 2.5) pellets match the SnSe structure with *Pnma* space group in both parallel (Fig. S7b) and normal (Fig. 3a) to the press direction. No secondary phases are observed within the detection limits of XRD. Lattice parameters expand with an increasing PbSe content, indicating the diffusion of Pb atoms into the SnSe matrix to form a solid solution of PbSe with the SnSe matrix. The expansion follows Vegard's law for solid solutions (Fig. 3b–c), and is consistent with the relatively larger size of the Pb^{2+} (1.19 Å) ion compared to Sn^{2+} (1.12 Å) ion. The expansion trend stabilizes at 2.5 mol% PbSe, indicating an overcoming of the solubility limit of Pb within SnSe. Additionally, the analysis of the relative intensities between the (4 0 0) and (1 1 1) peaks ($I_{(400)}/I_{(111)}$) in Fig. 3a, reveals a slight increase in the in-plane $I_{(400)}/I_{(111)}$ ratio with the PbSe content from 0 to 2.5 %, indicating slightly larger anisotropy in the SnSe-PbSe samples. We hypothesize that this could be attributed to the effects of alloying and the formation of nanometric secondary phases during the sintering process. During the sintering process, the material undergoes a densification and grain growth process. The presence of pinning centers (*i.e.* nanometric secondary phases) for grain boundary movement could promote the grains to preferentially orient in specific directions to increase the material density.

Upon annealing and consolidation, cross-section SEM micrographs show bare SnSe particles coalesce and grow into larger grains with sizes on the order of several microns (average grain size *ca.* 3.2 ± 1 μm) as shown in Fig. 3d–e, which is consistent with our previous reports [44,49]. When the powder contains PbSe NCs, the sintered pellets display much smaller grains than the bare SnSe, with smaller grains for those composites produced with larger quantities of PbSe, *e.g.* SnSe-2.5 %PbSe NCPs have an average grain size of 0.75 ± 0.2 μm. Significant differences in grain coarsening and growth are already noticeable after the annealing step, as can be seen in Fig. S8.

To further evaluate the microstructure of the NCPs, bare SnSe and SnSe-2.5 %PbSe pellets were thinned to electron transparency to produce a self-suspended lamella. Low magnification scanning transmission electron microscopy (STEM) images reveal significantly different

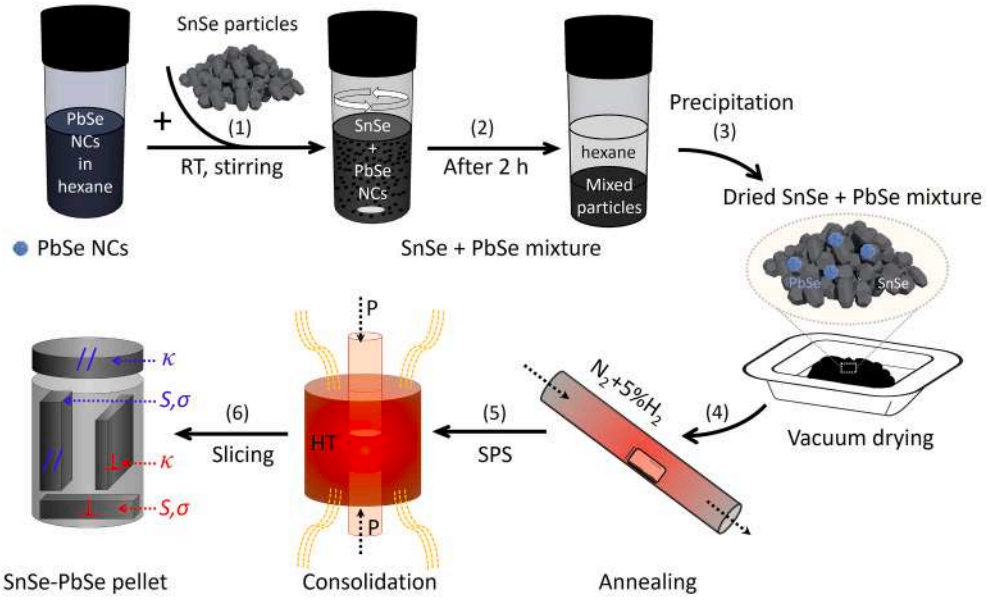

Fig. 1. Scheme of the fabrication process of bulk SnSe-PbSe NCPs. (1–2) blending the oleate-capped PbSe NCs with SnSe particles in hexane by stirring for *ca.* 2 h at room temperature; (3) purification and drying of the SnSe-PbSe particle blend; (4) annealing; (5) spark plasma sintering (SPS) for producing cylinders (Ø = 9 mm × h = 12 mm); and (6) slicing for the transport properties measurements of the bulk SnSe-PbSe NCPs.

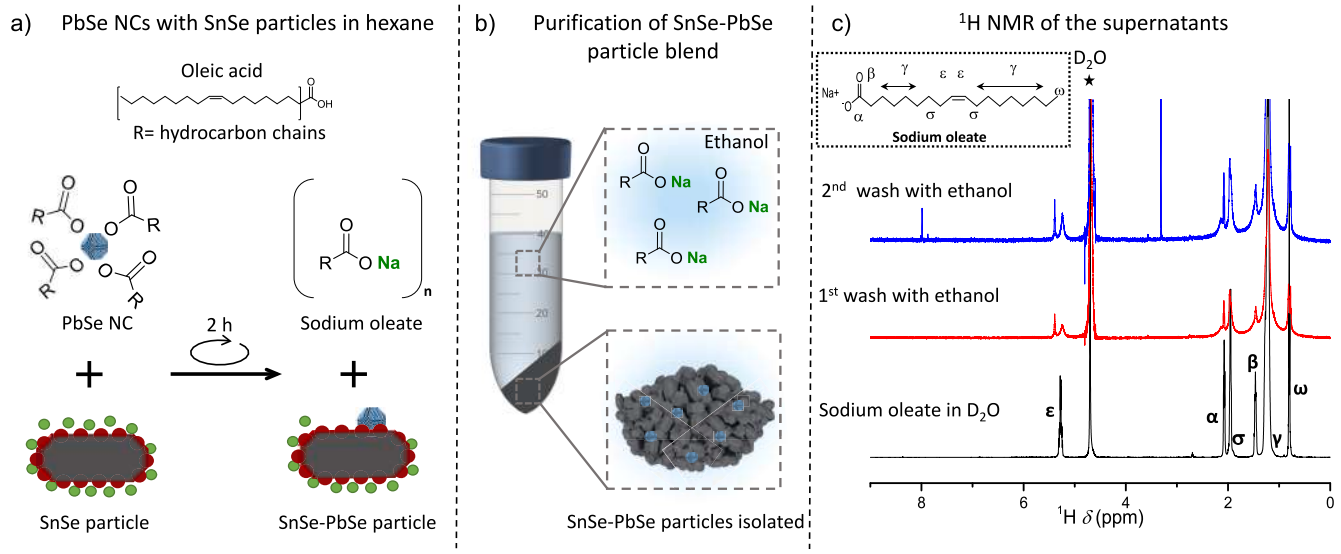

Fig. 2. (a) The reaction mechanism by the mixing SnSe powders with oleate-capped PbSe NCs, (b) illustration of the washing steps conducted, where sodium oleate is present in the supernatant and the SnSe-PbSe particles are isolated. c) ^{1}H NMR of the two supernatants collected after washing the SnSe-PbSe particles.

microstructures (Fig. S9). SnSe-2.5 %PbSe NCPs exhibits a larger density of grain boundaries, as well as different types of defects (Fig. 4, S9, and S10). In Fig. 4a, a high-resolution TEM (HRTEM) image showing the boundary area between three different grains is reported. Fig. 4b shows the corresponding frequency filtered map evidencing each of the three grains with a different color, in particular all the grains observed have been indexed as containing the SnSe crystal phase with orthorhombic *Pnma* space group oriented along different directions: [0 1 1] zone axis for the grain in blue, [1 1 2] zone axis for the grain in red and [1 2 5] zone axis for the grain in green as reported in Fig. 4c. The insets shown in Fig. 4a correspond to magnified details of each grain atomic structure, together with the corresponding superposed HRTEM simulated images, evidencing the perfect match between experimental and simulated crystal phases.

Upon closer examination of each grain structure, it becomes evident that there are discernible precipitates present, as reported in Fig. 4d and g. In both cases, we could isolate the nanoprecipitates in the frequency filtered maps reported in Fig. 4e and h, respectively. Here the precipitates are in green while the main grain structure is in red. Analyzing the corresponding power spectra, Fig. 4f and i, we identify their atomic arrangement, finding in both cases the PbSnSe orthorhombic *Pnma* crystalline structure along [1 0 1] and [1 2 3] zone axes, respectively. The fitting of the powder spectra with different structures, including PbSe cubic, PbSe *Pnma* and PbSnSe *Fm-3 m*, revealed that PbSnSe *Pnma* shows the best fit across all precipitates analyzed [52], as it gave us the smallest deviation error when comparing the experimental plane distances and relative angles with the simulated ones.

Based on the data obtained through HRTEM, we conclude that the SnSe-PbSe NCPs have PbSnSe nanoprecipitates, instead of the expected PbSe, produced during the thermal treatments. We hypothesize that the

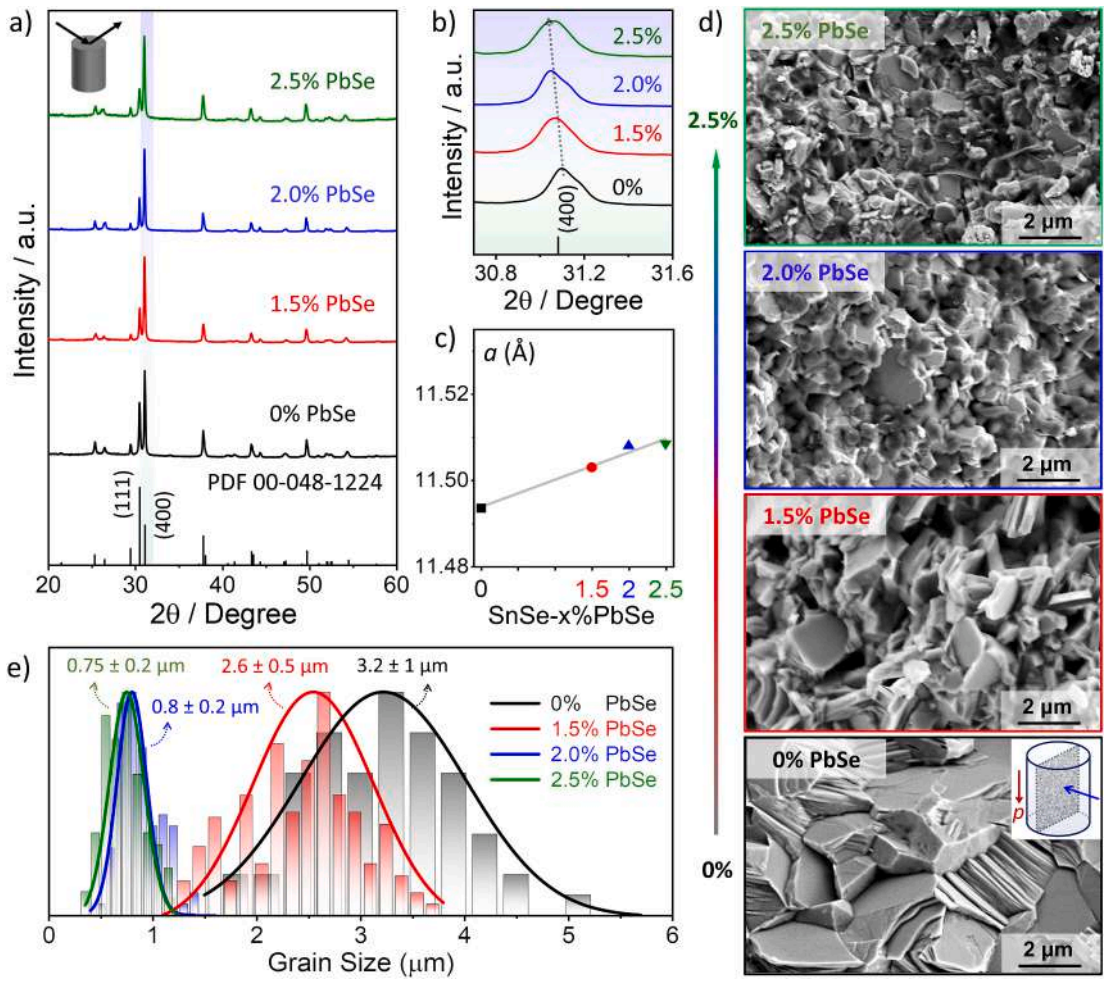

Fig. 3. (a) XRD patterns of the pellets obtained from SnSe-x%PbSe (x = 0, 1.5, 2.0, and 2.5) NCPs in the normal to the press direction, including SnSe reference pattern (PDF 00–048–1224). (b) Magnification of the (4 0 0) XRD peak at *ca.* 2θ = 31°. (c) Experimental lattice parameter "*a*" calculated from XRD patterns. (d) Cross-section SEM images of the pellets from SnSe-x%PbSe (x = 0, 1.5, 2.0, and 2.5) NCPs, and (e) the corresponding grain size distribution histograms and average size.

presence of such secondary phase nanoparticles in the polycrystalline material is the reason for grain growth inhibition in the SnSe-PbSe system, similar to what has been previously reported in SnSe-CdSe [44] and SnTe-Bi_2S_3 [53] systems, despite the differences in sample processing. The presence of a secondary phase at the grain boundary significantly diminishes the driving force for grain boundary migration, restricting grain growth. Such a phenomenon is known as the Zener pinning [54,55]. The amount of the secondary phase is directly related to the nominal content of added PbSe, considering a partial diffusion of Pb into the SnSe matrix to form an alloy [56]. This is evidenced by the fact that the sample with PbSe around 1.5 % does not show a significant reduction in grain size, as such content of PbSe is within the solubility limit of PbSe into SnSe. As we move beyond this solubility limit, and add more PbSe, more PbSnSe particles form as the second phase enhancing the pinning of the grain boundary movement.

3. Transport properties

The transport properties are measured along two directions: parallel and perpendicular to the pressure axis, as depicted in the schematic diagram in Fig. 1. The zT values along the parallel direction are larger than that along the normal direction [44,49]. Consequently, in the main text, we only display the transport properties in the parallel direction (Fig. 5 and S11). The measurements in the perpendicular direction, are shown in Fig. S12.

Bare SnSe and SnSe-x%PbSe (x = 1.5, 2.0, 2.5) pellets exhibit a positive S, which indicates a p-type transport (Fig. 5a), and the temperature dependence of S follows the expected trend for polycrystalline SnSe indicating no changes in the electronic structure [24,38,39,44,49]. *ab initio* density functional theory (DFT) calculations for the SnSe and $Sn_{0.98}Pb_{0.02}Se$ low temperature phase (*Pnma*) corroborate that Pb alloying does not perturb their electronic structure (Fig. S13). Hence, the difference in transport properties is mainly associated with the doping level and the scattering differences between the two materials.

The σ of both bare SnSe and SnSe-PbSe NCPs exhibits a thermally activated behavior, a common feature of polycrystalline SnSe (Fig. 5b) [10,15,16]. We attribute the high σ of bare SnSe to the content of Na acting as a dopant, resulting in high hole carrier concentration ($p_H > 10^{19}$ cm^{-3}) [44,49]. In comparison to the bare SnSe, σ values of the SnSe-x%PbSe NCPs are lower. This decline in σ is attributed to a simultaneous decrease in p_H and hall mobility (μ_H), as indicated by the Hall measurements (Fig. 5c, Table S2). The diminished carrier concentration can be ascribed to two phenomena: i) the decrease in the overall Na content in the composite compared to bare SnSe, and ii) the compensatory effect of Pb alloying, mitigating Sn vacancies [38].

The decrease in carrier mobility can be linked to the increase in grain boundary density. Samples containing PbSe have smaller grains and the presence of PbSnSe nanoprecipitates which introduce further electron scattering. Among these SnSe-x%PbSe (x = 1.5, 2.0, 2.5) samples, those with higher initial PbSe content exhibited slightly higher σ across the whole temperature range, which is mainly attributed to the smaller electronegativity difference between Pb and Se compared to Sn and Se,

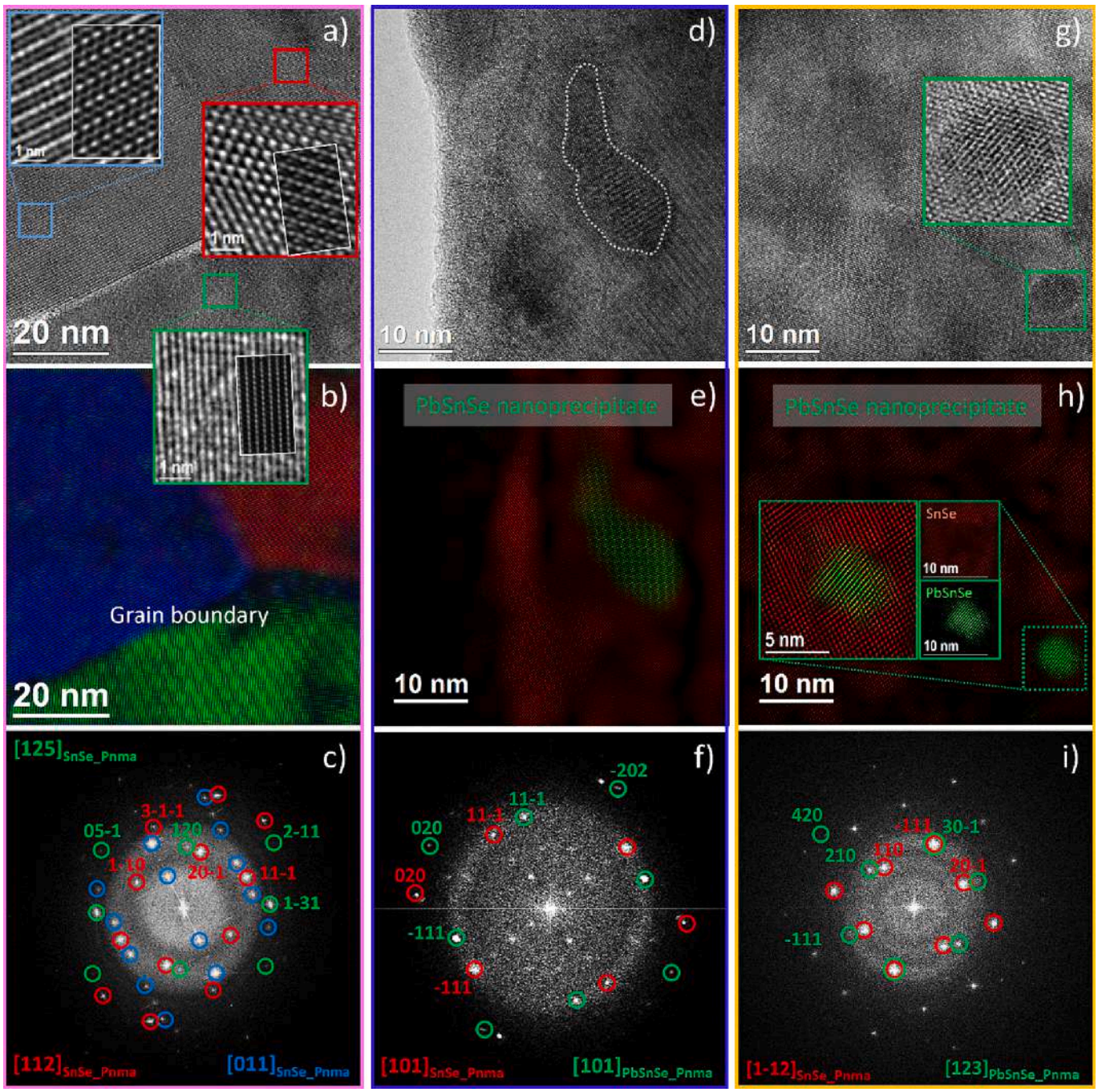

Fig. 4. (a-c) HRTEM micrographs of grain boundaries of SnSe matrix, and its respective power spectrum fitting with the orthorhombic phase. The inset in (a) shows the HRTEM images simulation of the SnSe domains. (d-f) PbSnSe NC crystallized in orthorhombic *Pnma* space group with the corresponding indexed power spectrum from the region marked in white and the phase images highlighting the PbSnSe NC (green) and the SnSe matrix (red). (g-i) A smaller PbSnSe NC crystallized in orthorhombic *Pnma* space group with the corresponding indexed power spectrum from the region marked in green, the inset in Fig. 4h shows the highlighting of another PbSnSe NC (green) and the SnSe matrix (red).

ensuring higher carrier concentration [42].

To understand the temperature dependent mobility data, we calculated the weighted mobility (μ_W) based on the measured σ and S [57], shown in Fig. S15. In the low-temperature range, the increase of μ_W with temperature indicates the presence of energy barriers (E_b) at the grain boundaries [58,59]. The energy barrier height (E_b; $\sigma \propto T^{-1/2} \exp(-E_b/k_BT)$) for the bare SnSe sample is determined to be ~141 meV, lower than ~189–217 meV for the SnSe-PbSe NCPs (Fig. S14). As the temperature increases, the effect of the potential barriers diminishes due to thermal carrier excitations at high temperature. Thus, the NCPs have similar σ to bare SnSe.

In all SnSe-x%PbSe (x = 0, 1.5, 2.0, 2.5) NCPs, temperature-dependent S peaks at *ca.* 650 K, indicating the onset for bipolar conduction. As the material gradually transitions from orthorhombic (*Pnma*) phase to the Cubic (*Cmcm*) phase, there is a change in the electronic structure, which is directly evidenced by the reduction of the energy band gap from 0.86 to 0.39 eV [32]. Once complete transformation to the *Cmcm* phase at temperatures above 800 K, the S and σ remain constant within the temperature range measured (Fig. S15). Our previous work demonstrated that the S of the solution-processed SnSe

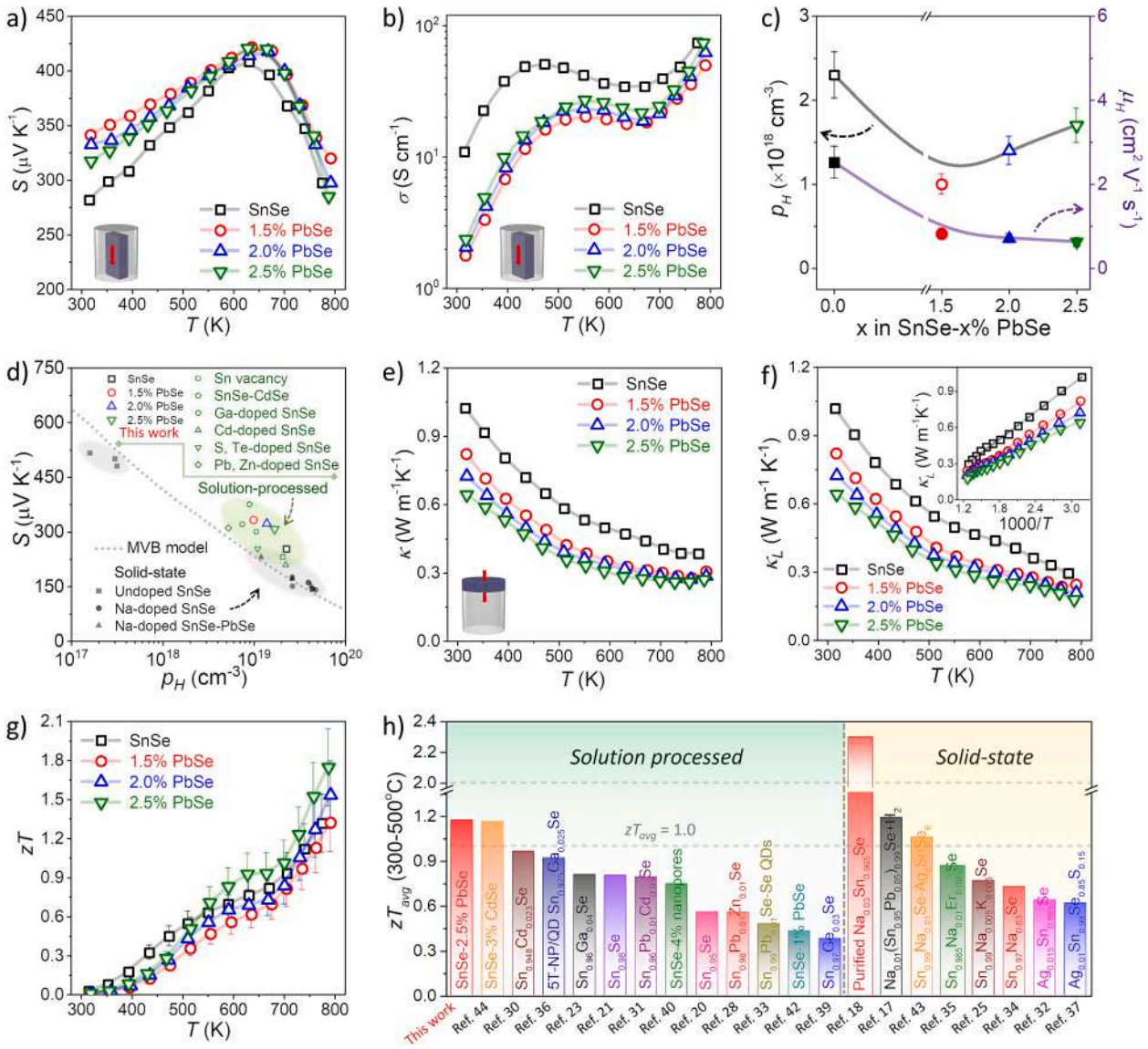

Fig. 5. Thermoelectric properties of SnSe-x%PbSe (x = 0, 1.5, 2.0, and 2.5). (a-c) Temperature dependence of (a) Seebeck coefficient (S), (b) electric conductivity (σ) and (c) ambient temperature Hall charge carrier concentration (p_H) and carrier mobility (μ_H). (d) Pisarenko plot at 300 K. Green dots are references from solution-processed materials [20,21,23,28,30,44,61], and black dots from solid-state synthetic methods [11,17,24,25,43,62,63]. The dashed line was calculated using a multiple band model (MVB) [60]. (e-g) Temperature dependence of (e) thermal conductivity (κ), (f) lattice thermal conductivity (κ_L), the inset shows the plot of 1000/T-dependent κ_L and (g) figure of merit (zT) values. (h) Comparison of zT_{avg} values of SnSe-2.5 %PbSe sample with reported state-of-the-art p-type polycrystalline SnSe: produced by solid-state technology [17,18,25,32,34,35,37,43], and solution-processed technology [20,21,23,28,30,31,33,36,39,40,42,44] in the mid-temperature range of 573 K to 773 K (300–500 °C).

matrix was higher than those reported for polycrystalline Na-doped counterparts synthesized by solid-state melting approach with similar carrier densities due to energy filtering effects [49]. The phenomenon resulting in such a larger *S*, is also effective in the SnSe-PbSe NCPs, as can be seen in the Pisarenko plot at 300 K, where all the *S* values lie above the line generated using a multiband model (Fig. 5d) [60]. In the Pisarenko plot, we juxtapose our results with previously reported experimental data [11,17,20,21,23–25,28,30,43,44,61–63]. The deviation from the Pisarenko line is ascribed to an augmented energy filtering effect, arising from the introduction of additional energy barriers by the presence of PbSnSe secondary phases. In essence, an effective potential barrier is established between the SnSe matrix and nanoprecipitates. Consequently, the low-energy charge carriers are filtered out, while the high-energy charge carriers can cross the potential barrier. The effect of the energy barriers decreases as the temperature increase, as can be observed in the temperature-dependent *S* values, where the difference in *S* values decreases between the bare SnSe and the SnSe-PbSe NCPs as the temperature increases.

All κ of the samples exhibit a consistent trend across the whole temperature range (Fig. 5e). The values of κ decrease with increasing temperature and then start to rise at high temperatures due to SnSe phase transition to the higher symmetry *Cmcm* phase. This behavior is consistent with temperature-dependent XRD measurements (Fig. S16). Notably, the κ values of SnSe-PbSe NCPs are lower than those of the SnSe matrix over the entire temperature range. These values are among the lowest values studied for conventional bulk polycrystalline SnSe-based materials at high temperatures (>700 K) [20,25,28,30,33,39,40,44,64].

The lattice thermal conductivity (κ_L) values are estimated according to $\kappa_L = \kappa - \kappa_e$ (Fig. 5f) with $\kappa_e = L_o \sigma T$, the Wiedemann–Franz law [65]. The specific heat (C_p), thermal diffusivity (λ), Lorentz number (L_o), and electronic thermal conductivity (κ_e) for all samples can be found in Fig. S17. At room temperature, κ_L decreases from *ca.*1.0 W $m^{-1}K^{-1}$ for

bare SnSe to 0.64 W $m^{-1}K^{-1}$ for SnSe-2.5 %PbSe NCPs This decreasing trend continues as the temperature increases, eventually reaching an ultra-low κ_L ~0.18 W $m^{-1}K^{-1}$, which is similar to the lowest reported value for polycrystalline SnSe [17,22,28,39,44]. The inset of Fig. 5f shows the curves of κ_L versus 1000/T for SnSe-x%PbSe NCPs, from which all κ_L values show a roughly linear relationship, indicating that Umklapp phonon scattering plays the most significant role in SnSe [30, 66,67]. Additionally, based on the above SEM and HRTEM characterization results, the extremely low κ in SnSe-PbSe NCPs is due to: i) high grain boundary density (smaller grain size), ii) the formation of atomic defects by Pb alloying, and iii) the presence of PbSnSe nanoprecipitates. These factors collectively contribute to the formation of defects spanning from atomic to nanometer to micrometer scales, which together build the all-scale hierarchical phonon scattering centers to efficiently scatter phonons with various mean free paths [68].

Overall, the significant reduced thermal conductivity contributed to a maximum zT (zT_{max}) value of 1.75 at 788 K for SnSe-2.5 %PbSe NCPs (Fig. 5g). Such a high TE performance positions our SnSe-2.5 %PbSe among the best-performing polycrystalline SnSe-based materials (Fig. S18). More importantly, it yields a high zT_{avg} value of *ca.* 1.2 in polycrystalline SnSe within the mid-temperature range from 573 to 773 K, as shown in Fig. 5h, according to following formula (1):

$$zT_{avg} = \frac{1}{T_h - T_c}\int_{T_c}^{T_h} zTdT \tag{1}$$

where T_h and T_c are the temperatures of the hot side and cold side, respectively. Given that polycrystalline SnSe is recognized as a mid-temperature TE material, it is suited for applications within this specified temperature range. The TE power generation efficiency (η) of actual devices depends on zT_{avg} based on the following relationship shown below (2) [69], and the η was estimated to be 5.6 % at a temperature difference of 200 K and cold-side temperature of 573 K for the SnSe-2.5 %PbSe sample.

$$\eta = \frac{T_h - T_c}{T_h}\left[\frac{\sqrt{1+zT_{avg}} - 1}{\sqrt{1+zT_{avg}} + \frac{T_c}{T_h}}\right] \tag{2}$$

Importantly, the results obtained from SnSe-PbSe NCPs exhibit remarkable stability, maintaining consistent performance during cycling tests and operation at high temperatures (Fig. S19, S20). Furthermore, the reproducibility of these results has been confirmed across multiple samples (Fig. S21).

4. Conclusions

In summary, we present a systematic bottom-up approach for the fabrication of compositionally controllable SnSe-PbSe NCPs through precisely mixing surfactant-free SnSe particles with oleate-capped PbSe NCs. The introduction of PbSe NCs during the annealing and consolidation steps modifies the electrical and thermal transport properties of the Na-doped SnSe matrix by partially removing Na from the SnSe particle surface, alloying with Pb to decrease Sn vacancies, increasing grain boundary density, and forming nanoprecipitates of the secondary phase PbSnSe. Such compositional and structural properties lead to significantly enhanced zTs, with peak values increasing from 1.32 at 773 K for the pure SnSe matrix to 1.75 at 788 K for SnSe-PbSe containing 2.5 mol% PbSe. More importantly, this work reports a cost-effective and stable material with one of the highest zT_{avg} of *ca.* 1.2 to date in the mid-temperature range in polycrystalline SnSe, contributing to the screening of promising *p*-type polycrystalline SnSe-based materials for future TE applications.

Credit authorship contribution statement

Yu Liu: Writing – original draft, Methodology, Data curation, Conceptualization. **Seungho Lee:** Writing – review & editing, Resources, Methodology, Data curation. **Christine Fiedler:** Writing – review & editing, Resources, Data curation. **Maria Chiara Spadaro:** Writing – review & editing, Software. **Cheng Chang:** Writing – review & editing, Software. **Mingquan Li:** Writing – review & editing. **Min Hong:** Writing – review & editing, Software. **Jordi Arbiol:** Writing – review & editing, Software. **Maria Ibáñez:** Writing – review & editing, Resources, Project administration, Funding acquisition.

Declaration of competing interest

The authors declare that they have no known competing financial interests or personal relationships that could have appeared to influence the work reported in this paper.

Data availability

Data will be made available on request.

Acknowledgments

The Scientific Service Units (SSU) of ISTA supported this research through resources provided by the Electron Microscopy Facility (EMF), NMR Facility, and the Lab Support Facility (LSF). Y.L., S.L., C.F., C.C. and M.I. acknowledge financial support from ISTA and the Werner Siemens Foundation. Y.L. acknowledges funding from the National Natural Science Foundation of China (NSFC) (Grants No. 22209034), the Innovation and Entrepreneurship Project of Overseas Returnees in Anhui Province (Grant No. 2022LCX002). C.C. acknowledges funding from the National Natural Science Foundation of China (NSFC) (Grants No. 12374023). ICN2 acknowledges funding from Generalitat de Catalunya 2021SGR00457. The authors thank support from the project NANOGEN(PID2020-116093RB-C43), funded by MCIN/ AEI/ 10.13039/501100011033/ and by "ERDF Away of making Europe", by the "European Union". ICN2 is supported by the Severo Ochoaprogram from Spanish MCIN / AEI (Grant No.: CEX2021-001214-S) and is funded by the CERCA Programme / Generalitat de Catalunya. ICN2 is founding member of e-DREAM [70].

Appendix A. Supplementary data

Supplementary data to this article can be found online at https://doi.org/10.1016/j.cej.2024.151405.

References

[1] X.L. Shi, J. Zou, Z.G. Chen, Advanced thermoelectric design: From materials and structures to devices, Chem. Rev. 120 (2020) 7399–7515.
[2] G. Tan, L.-D. Zhao, M.G. Kanatzidis, Rationally designing high-performance bulk thermoelectric materials, Chem. Rev. 116 (2016) 12123–12149.
[3] S. Ortega, M. Ibáñez, Y. Liu, Y. Zhang, M.V. Kovalenko, D. Cadavid, A. Cabot, Bottom-up engineering of thermoelectric nanomaterials and devices from solution-processed nanoparticle building blocks, Chem. Soc. Rev. 46 (2017) 3510–3528.
[4] Y. Liu, M. Ibáñez, Tidying up the mess, Science 371 (2021) 678–679.
[5] M. Kober, Holistic development of thermoelectric generators for automotive applications, J. Electron. Mater. 49 (2020) 2910–2919.
[6] S. Hooshmand Zaferani, M.W. Sams, X.-L. Shi, N. Mehrabian, R. Ghomashchi, Z.-G. Chen, applications of thermoelectric generators to improve catalytic-assisted hydrogen production efficiency: future directions, Energy & Fuels 36 (2022) 8096–8106.
[7] S. LeBlanc, Thermoelectric generators: Linking material properties and systems engineering for waste heat recovery applications, Sustain, Mater. Technol. 1–2 (2014) 26–35.
[8] S. Li, X. Li, Z. Ren, Q. Zhang, Recent progress towards high performance of tin chalcogenide thermoelectric materials, J. Mater. Chem. A 6 (2018) 2432–2448.
[9] L.-D. Zhao, C. Chang, G. Tan, M.G. Kanatzidis, SnSe: a remarkable new thermoelectric material, Energy Environ. Sci. 9 (2016) 3044–3060.

[10] X.-L. Shi, X. Tao, J. Zou, Z.-G.G. Chen, High-performance thermoelectric SnSe: Aqueous synthesis, innovations, and challenges, Adv. Sci. 7 (2020) 1902923.
[11] L.D. Zhao, S.H. Lo, Y. Zhang, H. Sun, G. Tan, C. Uher, C. Wolverton, V.P. Dravid, M. G. Kanatzidis, Ultralow thermal conductivity and high thermoelectric figure of merit in SnSe crystals, Nature 508 (2014) 373–377.
[12] C. Chang, M. Wu, D. He, Y. Pei, C.F. Wu, X. Wu, H. Yu, F. Zhu, K. Wang, Y. Chen, L. Huang, J.F. Li, J. He, L.D. Zhao, 3D charge and 2D phonon transports leading to high out-of-plane ZT in n-type SnSe crystals, Science 360 (2018) 778–783.
[13] B. Qin, D. Wang, X. Liu, Y. Qin, J.-F. Dong, J. Luo, J.-W. Li, W. Liu, G. Tan, X. Tang, J.-F. Li, J. He, L.-D. Zhao, Power generation and thermoelectric cooling enabled by momentum and energy multiband alignments, Science 373 (2021) 556–561.
[14] D. Liu, D. Wang, T. Hong, Z. Wang, Y. Wang, Y. Qin, L. Su, T. Yang, X. Gao, Z. Ge, B. Qin, L.-D. Zhao, Lattice plainification advances highly effective SnSe crystalline thermoelectrics, Science 380 (2023) 841–846.
[15] W. Shi, M. Gao, J. Wei, J. Gao, C. Fan, E. Ashalley, H. Li, Z. Wang, Tin selenide (SnSe): growth, properties, and applications, Adv. Sci. 5 (2018) 1700602.
[16] Z.-G. Chen, X. Shi, L.-D. Zhao, J. Zou, High-performance SnSe thermoelectric materials: Progress and future challenge, Prog. Mater. Sci. 97 (2018) 283–346.
[17] Y.K. Lee, Z. Luo, S.P. Cho, M.G. Kanatzidis, I. Chung, Surface oxide removal for polycrystalline SnSe reveals near-single-crystal thermoelectric performance, Joule 3 (2019) 719–731.
[18] C. Zhou, Y.K. Lee, Y. Yu, S. Byun, Z.-Z. Luo, H. Lee, B. Ge, Y.-L. Lee, X. Chen, J. Y. Lee, O. Cojocaru-Mirédin, H. Chang, J. Im, S.-P. Cho, M. Wuttig, V.P. Dravid, M. G. Kanatzidis, I. Chung, Polycrystalline SnSe with a thermoelectric figure of merit greater than the single crystal, Nat. Mater. 20 (2021) 1378–1384.
[19] A.K. Munirathnappa, H. Lee, I. Chung, Recent advances in ultrahigh thermoelectric performance material SnSe, Mater. Lab 2 (2023) 220056–220059.
[20] W. Wei, C. Chang, T. Yang, J. Liu, H. Tang, J. Zhang, Y. Li, F. Xu, Z. Zhang, J.-F. Li, G. Tang, Achieving high thermoelectric figure of merit in polycrystalline SnSe via introducing Sn vacancies, J. Am. Chem. Soc. 140 (2017) 499–505.
[21] X. Shi, Z.G. Chen, W. Liu, L. Yang, M. Hong, R. Moshwan, L. Huang, J. Zou, Achieving high figure of merit in p-type polycrystalline $Sn_{0.98}Se$ via self-doping and anisotropy-strengthening, Energy Storage Mater. 10 (2018) 130–138.
[22] X.-L. Shi, W.-D. Liu, M. Li, Q. Sun, S.-D. Xu, D. Du, J. Zou, Z.-G. Chen, A solvothermal synthetic environmental design for high-performance SnSe-based thermoelectric materials, Adv. Energy Mater. 12 (2022) 2200670.
[23] X. Lou, S. Li, X. Chen, Q. Zhang, H. Deng, J. Zhang, D. Li, X. Zhang, Y. Zhang, H. Zeng, G. Tang, Lattice strain leads to high thermoelectric performance in polycrystalline SnSe, ACS Nano 15 (2021) 8204–8215.
[24] T.-R. Wei, G. Tan, X. Zhang, C.-F. Wu, J.-F. Li, V.P. Dravid, G.J. Snyder, M. G. Kanatzidis, Distinct impact of alkali-ion doping on electrical transport properties of thermoelectric p-type polycrystalline SnSe, J. Am. Chem. Soc. 138 (2016) 8875–8882.
[25] Z.H. Ge, D. Song, X. Chong, F. Zheng, L. Jin, X. Qian, L. Zheng, R.E. Dunin-Borkowski, P. Qin, J. Feng, L.D. Zhao, Boosting the thermoelectric performance of (Na, K)-codoped polycrystalline SnSe by synergistic tailoring of the band structure and atomic-scale defect phonon scattering, J. Am. Chem. Soc. 139 (2017) 9714–9720.
[26] C.L. Chen, H. Wang, Y.Y. Chen, T. Day, G.J. Snyder, Thermoelectric properties of p-type polycrystalline SnSe doped with Ag, J. Mater. Chem. A 2 (2014) 11171–11176.
[27] X. Shi, K. Zheng, M. Hong, W. Liu, R. Moshwan, Y. Wang, X. Qu, Z.G. Chen, J. Zou, Boosting the thermoelectric performance of p-type heavily Cu-doped polycrystalline SnSe via inducing intensive crystal imperfections and defect phonon scattering, Chem. Sci. 9 (2018) 7376–7389.
[28] J. Liu, P. Wang, M. Wang, R. Xu, J. Zhang, J. Liu, D. Li, N. Liang, Y. Du, G. Chen, G. Tang, Achieving high thermoelectric performance with Pb and Zn codoped polycrystalline SnSe via phase separation and nanostructuring strategies, Nano Energy 53 (2018) 683–689.
[29] X. Wang, J. Xu, G.-Q. Liu, X. Tan, D. Li, H. Shao, T. Tan, J. Jiang, Texturing degree boosts thermoelectric performance of silver-doped polycrystalline SnSe, NPG Asia Mater. 9 (2017) e426.
[30] X. Shi, A. Wu, T. Feng, K. Zheng, W. Liu, Q. Sun, M. Hong, S.T. Pantelides, Z.-G. Chen, J. Zou, High thermoelectric performance in p-type polycrystalline Cd-doped SnSe achieved by a combination of cation vacancies and localized lattice engineering, Adv. Energy Mater. 9 (2019) 1803242.
[31] S. Li, X. Lou, X. Li, J. Zhang, D. Li, H. Deng, J. Liu, G. Tang, Realization of high thermoelectric performance in polycrystalline tin selenide through schottky vacancies and endotaxial nanostructuring, Chem. Mater. 32 (2020) 9761–9770.
[32] L. Zhang, J. Wang, Q. Sun, P. Qin, Z. Cheng, Z. Ge, Z. Li, S. Dou, Three-stage inter-orthorhombic evolution and high thermoelectric performance in Ag-doped nanolaminar SnSe polycrystals, Adv. Energy Mater. 7 (2017) 1700573.
[33] R. Xu, L. Huang, J. Zhang, D. Li, J. Liu, J. Liu, J. Fang, M. Wang, G. Tang, Nanostructured SnSe integrated with Se quantum dots with ultrahigh power factor and thermoelectric performance from magnetic field-assisted hydrothermal synthesis, J. Mater. Chem. A 7 (2019) 15757–15765.
[34] S. Liang, J. Xu, J.G. Noudem, H. Wang, X. Tan, G.-Q. Liu, H. Shao, B. Yu, S. Yue, J. Jiang, Thermoelectric properties of textured polycrystalline $Na_{0.03}Sn_{0.97}Se$ enhanced by hot deformation, J. Mater. Chem. A 6 (2018) 23730–23735.
[35] B. Su, Z. Han, Y. Jiang, H.-L. Zhuang, J. Yu, J. Pei, H. Hu, J.-W. Li, Y.-X. He, B.-P. Zhang, J.-F. Li, Re-doped p-Type thermoelectric SnSe polycrystals with enhanced power factor and high ZT > 2, Adv. Funct. Mater. 33 (2023) 2301971.
[36] S. Li, Y. Hou, S. Zhang, Y. Gong, S. Siddique, D. Li, J. Fang, P. Nan, B. Ge, G. Tang, Realizing high thermoelectric performance in magnetic field-assisted solution synthesized nanoporous SnSe integrated with quantum dots, Chem. Eng. J. 451 (2023) 138637.
[37] C.-C. Lin, R. Lydia, J.H. Yun, H.S. Lee, J.S. Rhyee, Extremely low lattice thermal conductivity and point defect scattering of phonons in Ag-doped $(SnSe)_{1-x}(SnS)_x$ compounds, Chem. Mater. 29 (2017) 5344–5352.
[38] Y.K. Lee, K. Ahn, J. Cha, C. Zhou, H.S. Kim, G. Choi, S.I. Chae, J.H. Park, S.P. Cho, S.H. Park, Y.E. Sung, W.B. Lee, T. Hyeon, I. Chung, Enhancing p-type thermoelectric performances of polycrystalline SnSe via tuning phase transition temperature, J. Am. Chem. Soc. 139 (2017) 10887–10896.
[39] S. Chandra, K. Biswas, Realization of high thermoelectric figure of merit in solution synthesized 2D SnSe nanoplates via Ge alloying, J. Am. Chem. Soc. 141 (2019) 6141–6145.
[40] X. Shi, A. Wu, W. Liu, R. Moshwan, Y. Wang, Z.-G. Chen, J. Zou, Polycrystalline SnSe with extraordinary thermoelectric property via nanoporous design, ACS Nano 12 (2018) 11417–11425.
[41] H.X. Wang, L.S. Mao, X.J. Tan, G.Q. Liu, J.T. Xu, H.Z. Shao, H.Y. Hu, J. Jiang, Nontrivial thermoelectric behavior in cubic SnSe driven by spin-orbit coupling, Nano Energy 51 (2018) 649–655.
[42] G. Tang, W. Wei, J. Zhang, Y. Li, X. Wang, G. Xu, C. Chang, Z. Wang, Y. Du, L. D. Zhao, Realizing High Figure of Merit in Phase-Separated Polycrystalline $Sn_{1-x}Pb_xSe$, J. Am. Chem. Soc. 138 (2016) 13647–13654.
[43] Y. Luo, S. Cai, X. Hua, H. Chen, Q. Liang, C. Du, Y. Zheng, J. Shen, J. Xu, C. Wolverton, V.P. Dravid, Q. Yan, M.G. Kanatzidis, High thermoelectric performance in polycrystalline SnSe via dual-doping with Ag/Na and nanostructuring with Ag_8SnSe_6, Adv. Energy Mater. 9 (2019) 1803072.
[44] Y. Liu, M. Calcabrini, Y. Yu, S. Lee, C. Chang, J. David, T. Ghosh, M.C. Spadaro, C. Xie, O. Cojocaru-Mirédin, J. Arbiol, M. Ibáñez, Defect engineering in solution-processed polycrystalline SnSe leads to high thermoelectric performance, ACS Nano 16 (2022) 78–88.
[45] S. Chandra, P. Dutta, K. Biswas, High-performance thermoelectrics based on solution-grown SnSe nanostructures, ACS Nano 16 (2022) 7–14.
[46] C. Fiedler, T. Kleinhanns, M. Garcia, S. Lee, M. Calcabrini, M. Ibáñez, Solution-processed inorganic thermoelectric materials: Opportunities and challenges, Chem. Mater. 34 (2022) 8471–8489.
[47] T. Kleinhanns, F. Milillo, M. Calcabrini, C. Fiedler, S. Horta, D. Balazs, M. J. Strumolo, R. Hasler, J. Llorca, M. Tkadletz, R.L. Brutchey, M. Ibáñez, A route to high thermoelectric performance: solution-based control of microstructure and composition in Ag_2Se, Adv. Energy Mater. n/a (2024) 2400408.
[48] G. Han, S.R. Popuri, H.F. Greer, J.W.G. Bos, W. Zhou, A.R. Knox, A. Montecucco, J. Siviter, E.A. Man, M. MacAuley, D.J. Paul, W.G. Li, M.C. Paul, M. Gao, T. Sweet, R. Freer, F. Azough, H. Baig, N. Sellami, T.K. Mallick, D.H. Gregory, Facile surfactant-free synthesis of p-type SnSe nanoplates with exceptional thermoelectric power factors, Angew. Chemie. Int. Ed. 55 (2016) 6433–6437.
[49] Y. Liu, M. Calcabrini, Y. Yu, A. Genç, C. Chang, T. Costanzo, T. Kleinhanns, S. Lee, J. Llorca, O. Cojocaru-Mirédin, M. Ibáñez, The importance of surface adsorbates in solution-processed thermoelectric materials: The case of SnSe, Adv. Mater. 33 (2021) 2106858.
[50] D.M. Balazs, B.M. Matysiak, J. Momand, A.G. Shulga, M. Ibáñez, M.V. Kovalenko, B.J. Kooi, M.A. Loi, Electron mobility of 24 $cm^2 V^{-1} s^{-1}$ in PbSe colloidal-quantum-dot superlattices, Adv. Mater. 30 (2018) 1802265.
[51] L. Protesescu, M. Nachtegaal, O. Voznyy, O. Borovinskaya, A.J. Rossini, L. Emsley, C. Copéret, D. Günther, E.H. Sargent, M.V. Kovalenko, Atomistic description of thiostannate-capped CdSe nanocrystals: retention of four-coordinate SnS_4 motif and preservation of Cd-rich stoichiometry, J. Am. Chem. Soc. 137 (2015) 1862–1874.
[52] S.V. Ovsyannikov, V.V. Shchennikov, A.Y. Manakov, A.Y. Likhacheva, I.F. Berger, A.I. Ancharov, M.A. Sheromov, High-pressure X-ray diffraction study of ternary and non-stoichiometric PbTe and PbSe crystals, Phys. Status Solidi 244 (2007) 279–284.
[53] C. Chang, Y. Liu, S. Ho Lee, M. Chiara Spadaro, K.M. Koskela, T. Kleinhanns, T. Costanzo, J. Arbiol, R.L. Brutchey, M. Ibáñez, Surface functionalization of surfactant-free particles: A strategy to tailor the properties of nanocomposites for enhanced thermoelectric performance, Angew. Chemie Int. Ed. 61 (2022) e202207002.
[54] E. Nes, N. Ryum, O. Hunderi, On the Zener drag, Acta Metall. 33 (1985) 11–22.
[55] M. Pa, M. Ferry, T. Chandra, Five decades of the Zener equation, ISIJ Int. 38 (1998) 913–924.
[56] P. Villars, Handbook of ternary alloy phase diagrams, ASM Int. 7 (1995) 8754–8755.
[57] G.J. Snyder, A.H. Snyder, M. Wood, R. Gurunathan, B.H. Snyder, C. Niu, Weighted mobility, Adv. Mater. 32 (2020) 2001537.
[58] J.J. Kuo, S.D. Kang, K. Imasato, H. Tamaki, S. Ohno, T. Kanno, G.J. Snyder, Grain boundary dominated charge transport in Mg_3Sb_2-based compounds, Energy Environ. Sci. 11 (2018) 429–434.
[59] J.Y.W. Seto, The electrical properties of polycrystalline silicon films, J. Appl. Phys. 46 (1975) 5247–5254.
[60] G. Shi, E. Kioupakis, Quasiparticle band structures and thermoelectric transport properties of p-type SnSe, J. Appl. Phys. 117 (2015) 065103.
[61] L. Huang, G. Han, B. Zhang, D.H. Gregory, Anion-exchange synthesis of thermoelectric layered $SnS_{0.1}Se_{0.9-x}Te_x$ nano/microstructures in aqueous solution: Complexity and carrier concentration, J. Mater. Chem. C 7 (2019) 7572–7579.
[62] L.-D. Zhao, G. Tan, S. Hao, J. He, Y. Pei, H. Chi, H. Wang, S. Gong, H. Xu, V. P. Dravid, C. Uher, G.J. Snyder, C. Wolverton, M.G. Kanatzidis, Ultrahigh power factor and thermoelectric performance in hole-doped single-crystal SnSe, Science 351 (2016) 141–144.
[63] E.K. Chere, Q. Zhang, K. Dahal, F. Cao, J. Mao, Z. Ren, Studies on thermoelectric figure of merit of Na-doped p-type polycrystalline SnSe, J. Mater. Chem. A 4 (2016) 1848–1854.

[64] Y. Gong, C. Chang, W. Wei, J. Liu, W. Xiong, S. Chai, D. Li, J. Zhang, G. Tang, Extremely low thermal conductivity and enhanced thermoelectric performance of polycrystalline SnSe by Cu doping, Scr. Mater. 147 (2018) 74–78.
[65] M. Hong, Z.G. Chen, L. Yang, T.C. Chasapis, S.D. Kang, Y. Zou, G.J. Auchterlonie, M.G. Kanatzidis, G.J. Snyder, J. Zou, Enhancing the thermoelectric performance of $SnSe_{1-x}Te_x$ nanoplates through band engineering, J. Mater. Chem. A 5 (2017) 10713–10721.
[66] D.R. Clarke, Materials selection guidelines for low thermal conductivity thermal barrier coatings, Surf. Coatings Technol. 163–164 (2003) 67–74.
[67] K. Peng, X. Lu, H. Zhan, S. Hui, X. Tang, G. Wang, J. Dai, C. Uher, G. Wang, X. Zhou, Broad temperature plateau for high ZTs in heavily doped p-type SnSe single crystals, Energy Environ. Sci. 9 (2016) 454–460.
[68] K. Biswas, J. He, I.D. Blum, C.I. Wu, T.P. Hogan, D.N. Seidman, V.P. Dravid, M. G. Kanatzidis, High-performance bulk thermoelectrics with all-scale hierarchical architectures, Nature 489 (2012) 414–418.
[69] D.M. Rowe, Thermoelectrics handbook: macro to nano, CRC Press, 2018.
[70] R. Ciancio, R.E. Dunin-Borkowski, E. Snoeck, M. Kociak, R. Holmestad, J. Verbeeck, A.I. Kirkland, G. Kothleitner, J. Arbiol, e-DREAM: the european distributed research infrastructure for advanced electron microscopy, Microsc. Microanal. 28 (2022) 2900–2902.